Elastic continuum theory of the structure and dynamics of uniaxially incommensurate monolayer solids

L. W. Bruch

Department of Physics, University of Wisconsin–Madison, Madison, Wisconsin 53706
(Received 16 December 1992)

A systematic development is given, within the elastic continuum approximation, of the properties of monolayer solids with parallel arrays of domain walls. The external potentials correspond to cases of monatomic adsorbates on the basal-plane surface of graphite and on an fcc(111) surface with distinct energies at the fcc and hcp stacking sites. Heavy and superheavy domain walls (also light and superlight walls) are treated. The harmonic-frequency spectra are determined, with some cases of anomalous dispersion and of dynamic instability. The Debye approximation to the specific heat is developed for the adsorbate on the graphite substrate.

I. INTRODUCTION

A monolayer solid in the presence of a spatially periodic external potential may have extended regions (domains) which are commensurate with the external potential, and which are separated by narrow regions (walls) in which the misfit is concentrated.[1] Such phenomena were studied first with one-dimensional models, the Frenkel-Kontorova discrete chain[2] of atoms in a sinusoidal potential and the Frank–van der Merwe[3] continuum approximation to the Frenkel-Kontorova chain. The extension to planar monolayers began with quasi-one-dimensional models of parallel straight walls,[4] the striped phases, in which the displacement vectors relative to commensurate sites had only one nonzero component. The modeling was then generalized to two-dimensional configurations in which the domain walls form honeycomb lattices[5] or striped lattices with two-component displacement vectors.[6,7]

Here a systematic development is given, within the elastic continuum approximation,[8] of the properties of monolayer solids with parallel arrays of domain walls. Two classes of external potential are treated: (i) the holding potential of monatomic adsorbates on the basal-plane surface of graphite, a triangular lattice of potential minima; and (ii) the corresponding potential for the (111) surface of a face-centered-cubic solid with two sets of threefold sites which are nearly degenerate potential minima.[7,9–11] The optimal configuration and minimum potential energy of the adlayer are determined for alternative ways[12] of achieving the same net misfit. The structure and harmonic dynamics of the compressed solid ("heavy" walls) and the dilated solid ("light" walls) are closely related. The results are analyzed in terms of energies of wall-wall interactions.[1] The relative stability of what are termed[12] "heavy" and "superheavy" walls (or, "light" and "superlight") is determined for the static solutions. Then the harmonic-frequency spectrum[13] is derived for small-amplitude oscillations about the optimized static configurations. A merit of the elastic continuum approximation is that the problem can be expressed

in a scaled form, where the results depend on only a few dimensionless parameters: the misfit, an elastic constant ratio, and a reduced wave vector for the frequency. Although the language of "domain walls' focuses attention on only a few degrees of freedom of the monolayer, the model calculations do treat the full nonuniform layer.

The results are based mostly on detailed numerical solutions, although analytical results[3,14,15] are available to test the methods in special cases. The analysis is less explicit than in a previous paper,[18] which developed analytical approximations for the static properties of isolated domain walls, using variational methods. The reliance on computational results follows from the need to track small energy increments for the wall-wall interactions and to have precise static solutions for the force field in the dynamics calculations.

This work extends applications[1,3,4,7,8,16] of the elastic continuum approximation by (i) treating more complex two-dimensional structures and the effect of different adsorption energies[9,10,16] at the fcc and hcp stacking sites of an fcc(111) surface; (ii) examining the relative energy[8,16] of heavy and superheavy structures as a function of misfit; (iii) determining the dispersion relation[13,14] of the normal modes; and (iv) developing the Debye theory[17] of the thermodynamics of the nonuniform monolayer. The stability of the structures is tested using both the static energies of the structures and the dynamics of small-amplitude distortions, normal modes. The limitations of the analysis are that (i) only striped configurations are treated, and (ii) effects of thermal disordering,[18,19] such as melting of lattices, are omitted.

There are several significant simplifying assumptions. The external potential, or the substrate in the adsorption problem, is taken to be rigid; thus long-range interactions between walls which arise from elastic distortions of the substrate[9] are neglected. The configurations are determined by potential-energy minimization, and the wall-wall interactions are purely mechanical energies. At finite temperatures and very small mean misfits, the entropic interactions for an adlayer on a rigid substrate, described by Coppersmith *et al.*[18] and by Pokrovsky and

                                   <u>48</u>   1765

Talapov,[19] dominate over the mechanical interactions.

The principal analytic results available for the elastic continuum approximation are for the static structure[3] and the harmonic-frequency spectrum[14] of the one-dimensional Frank–van der Merwe model. Solutions for the static structure of atomistic monolayer models have been given in several cases corresponding to adsorption on graphite,[5,20] and in a case of the fcc(111) model with degenerate fcc and hcp stacking sites.[6] The harmonic-frequency spectrum has been evaluated for some atomistic models.[6,13,21]

There have been a few observations of striped monolayer solids. There are structural signatures for hydrogen/graphite[22] and for xenon/platinum (111).[23] An excitation of domain-wall vibrations may have been observed[24] with inelastic neutron scattering from deuterium/graphite. The striped phase is inferred as one of the monolayer solid phases of helium/graphite; there are specific-heat data for that part of the phase diagram.[25] The reconstructed surface of gold(111) (Ref. 26) has a striped phase, with unequal sized domains centered on fcc and hcp stacking sites, and a herringbone superstructure. The striped phase also occurs for bromine intercalated in graphite.[27]

The organization of this paper is as follows: Section II contains the formulation of the calculations. Section III contains results for the static configurations, and Sec. IV contains results for the normal-mode frequencies of the nonuniform layers. Section V contains concluding remarks. Analytic results for the superheavy wall of monatomics/graphite are collected in Appendix A.

II. FORMULATION

A two-dimensional elastic continuum approximation is developed[1,8] for the adlayer motions in a plane at a perpendicular distance z_0 from the substrate. The potential energy is the sum of the elastic energy of the adlayer and the adlayer/substrate (holding potential) energy. These terms are formulated in Secs. II A and II B, respectively, with some comments on the values for parameter ratios which appear in the expressions. The lateral average of the adatom/substrate potential sets the height z_0 of the plane of two-dimensional motions, but does not enter explicitly into the rest of the work. The geometry of the uniaxially incommensurate layer is defined in Sec. II C, and the total energy is stated in terms of the displacements of atoms from commensurate sites. Scaled equations determining the minimum energy configuration and the normal modes of small amplitude oscillations are given in Secs. II D and II E.

A. Elastic energy

The elastic continuum energy for an isotropic two-dimensional solid with vector displacement **u** is[17]

$$\Delta E_{el} = \int d^2 r \{ -\phi[\partial_x u_x + \partial_y u_y]$$
$$+ \tfrac{1}{2}\Gamma_{11}[(\partial_x u_x)^2 + (\partial_y u_y)^2]$$
$$+ \tfrac{1}{2}\Gamma_{33}[\partial_x u_y + \partial_y u_x]^2 + \Gamma_{12}\partial_x u_x \partial_y u_y \}$$

$$(2.1)$$

in terms of the spreading pressure ϕ and pressure-renormalized elastic constants Γ_{11}, Γ_{12}, and Γ_{33}, which satisfy

$$\Gamma_{11} = \Gamma_{12} + 2\Gamma_{33} . \qquad (2.2)$$

The speeds of longitudinal and transverse sound in the uniform medium of mass density ρ are given by

$$c_l^2 = \Gamma_{11}/\rho, \quad c_t^2 = \Gamma_{33}/\rho . \qquad (2.3)$$

The ratio

$$A = 3\Gamma_{33}/\Gamma_{11} \qquad (2.4)$$

is a measure of the relative contribution of shearing motions in distortions of the monolayer. The fact that the bulk modulus is positive sets upper bounds $A \leq 3$ and $c_t \leq c_l$. A Cauchy solid[17] at zero spreading pressure has $A = 1$; model solids with Lennard-Jones pair potentials generally have[8] A in the range 1–2. Experimental data place A near 1 for H_2/graphite,[28] and in the range 0.4–0.7 for He/graphite.[17]

B. Holding potential

A model for the lateral variation of the adatom/substrate potential is[9]

$$V(\mathbf{r},z) = 2 \sum_{j=1}^{3} V_R(z) \cos(\mathbf{g}_j \cdot \mathbf{r}) - V_I(z) \sin(\mathbf{g}_j \cdot \mathbf{r}) . \qquad (2.5)$$

The orientation of the substrate surface reciprocal-lattice vectors $\mathbf{g}_1$, $\mathbf{g}_2$, and $\mathbf{g}_3$ relative to primitive vectors $\mathbf{a}_1$, $\mathbf{a}_2$, and $\mathbf{a}_3$ of the surface mesh is shown in Fig. 1. The vectors $\mathbf{g}_j$ have magnitude $g_0 = 4\pi/\sqrt{3}L$; the length L of the primitive vectors $\mathbf{a}_j$ is the nearest-neighbor spacing of atoms in the fcc(111) surface or the lattice constant (2.46 Å) of the graphite surface. The origin of the x,y coordinates is at a corner of the surface unit cell. An assumption in using Eq. (2.5) is that only the leading Fourier component of the potential is significant.

The model permits a distinction[9–11] in the adsorption

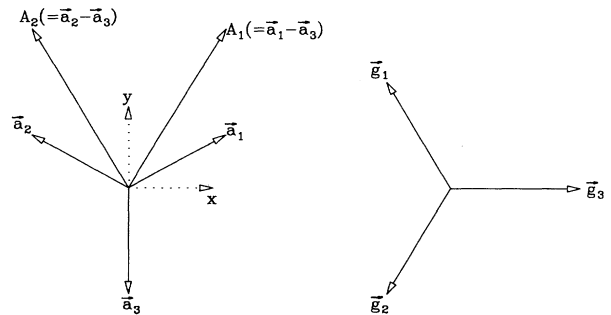

FIG. 1. Coordinate system, primitive vectors, and reciprocal-lattice vectors. Primitive vectors $\mathbf{a}_1$, $\mathbf{a}_2$, and $\mathbf{a}_3$ of the surface mesh and A_1 and A_2 of the $\sqrt{3}$ commensurate lattice are shown, as well as Cartesian axes $\hat{x}$ and $\hat{y}$. The orientation of the reciprocal-lattice vectors $\mathbf{g}_1$, $\mathbf{g}_2$, and $\mathbf{g}_3$ relative to these axes is shown at the right.

energy at the hexagonal-close-packed (hcp) and face-centered-cubic (fcc) stacking sites of the (111) face of a fcc solid. These two sets of sites, at $\rho_1 = (\frac{1}{3})(\mathbf{a}_1 - \mathbf{a}_2)$ and $\rho_2 = 2\rho_1$ in the unit cell, have equal energy for $V_I = 0$.

The model used here for graphite (GR) has $V_I = 0$; then the two sites in the unit cell atop the surface carbon atoms have equal energy. If the sites of minimum energy V are at the centers of carbon hexagons, vertices of the surface lattice, the amplitude $V_R(z_0)$ at the minimum of the holding potential is negative, and is written as $-V_g$.

For physical adsorption, the V_I term of the fcc(111) model arises from the first underlying layer; it is believed to be smaller than the V_R term by a factor of 10^{-3}–10^{-4}. When the potential minima are at ρ_1 or ρ_2, $V_R(z_0)$ is positive.

The two-dimensional approximation for the adlayer arises when the minimum of the adatom/substrate potential is sharp enough that adatom motions are restricted to the plane $z = z_0$. Such is assumed to be the case here.

C. Commensurate and uniaxially incommensurate lattices

Positions in the commensurate $\sqrt{3}R$ 30° lattice,[1] with primitive vectors $\mathbf{A}_1$ and $\mathbf{A}_2$ of length $L\sqrt{3}$, oriented as shown in Fig. 1, are given by ρ_0:

$$\mathbf{R}_c(j_1, j_2) = \rho_0 + j_1 \mathbf{A}_1 + j_2 \mathbf{A}_2 , \tag{2.6}$$

where j_1 and j_2 are integers, and ρ_0 sets the placement relative to the origin of the substrate surface unit cell. Similarly, positions in the incommensurate lattice are given by

$$\mathbf{R}(j_1, j_2) = \rho_0 + j_1 \mathbf{A}_1 + j_2 \mathbf{A}_2 + \mathbf{u}(j_1, j_2) . \tag{2.7}$$

The GR model has $\rho_0 = 0$; the corresponding fcc(111) model has $\rho_0 = \rho_1$. For the uniaxially incommensurate lattice, the function $\mathbf{u}$ is constant along rows of the commensurate lattice. For vectors oriented as in Fig. 1, $\mathbf{u}$ depends only on the combination $j_1 + j_2$. The increment in $\mathbf{u}$ for the superheavy/superlight wall[12] is $\pm\mathbf{a}_3$ after M rows, with a fractional misfit of $\pm 2/(3M)$. The increment in $\mathbf{u}$ for the heavy/light wall[12] is $\pm(-\mathbf{a}_1)$ or $\pm(-\mathbf{a}_2)$ after M rows, with a fractional misfit of $\pm 1/(3M)$.

This development is for uniaxial incommensurate lattices derived from the $\sqrt{3}R$ 30° commensurate lattice, which arises in several cases of physisorption. The results apply, with some relabeling of coordinates, to lattices derived from the 1×1 commensurate lattice on the fcc(111) substrate,[7] e.g., for Au(111).

These incommensurate lattices have equilibrium positions satisfying $\mathbf{u} = \mathbf{u}(y)$, uniaxial compression along the y axis. The formalism adapts easily to the case[7] of uniaxial compression along the x axis, $\mathbf{u} = \mathbf{u}(x)$. The case of uniaxial compression along an arbitrary axis $\mathbf{n}$, $\mathbf{u} = \mathbf{u}(\mathbf{n} \cdot \mathbf{r})$, is discussed briefly in Secs. III A and IV A.

The continuum approximation for the change in the adlayer/substrate potential energy relative to the commensurate state value is, for the Cartesian axes shown in Fig. 1,

$$V_{\text{lat}} = (2V_g/a_c)$$
$$\times \int d^2r [3\cos(\theta) - \cos(g_0 u_x + \theta)$$
$$- 2\cos(g_x u_x - \theta)\cos(g_y u_y)] , \tag{2.8}$$

where

$$g_x = g_0/2, \quad g_y = (g_0/2)\sqrt{3}, \quad \text{and} \quad a_c = (3L^2/2)\sqrt{3} . \tag{2.9}$$

The phase angle θ is zero for the GR model.

For the fcc(111) model, the parameters in Eq. (2.8) are

$$V_g = \sqrt{(V_R^2 + V_I^2)}, \quad \tan(\psi) = -V_I/V_R ,$$
and   (2.10)
$$\theta = \pi/3 - \psi .$$

The difference in energy $V(\mathbf{r}, z_0)$ between the hcp and fcc sites is

$$V(\rho_2, z_0) - V(\rho_1, z_0) = 6\sqrt{3} V_g \sin(\psi) , \tag{2.11}$$

and the difference between a saddle point $\mathbf{r}_s = (\frac{1}{2})(\mathbf{a}_1 - \mathbf{a}_2)$ and the site ρ_1 is

$$V(\mathbf{r}_s, z_0) - V(\rho_1, z_0) = 2V_g[3\cos(\theta) - \cos(3\psi)] . \tag{2.12}$$

The phase ψ is of the order of 10^{-3}–10^{-4} rad for model potentials in physical adsorption.

D. Minimum potential-energy configurations

The theory is developed in terms of parameters

$$V_0 = 2V_g/a_c \quad \text{and} \quad \gamma = g_y^2 V_0/\Gamma_{11} , \tag{2.13a}$$

a dimensionless length Y along the direction $(\mathbf{a}_3)$ of uniaxial compression, and scaled displacement functions:

$$Y = y\sqrt{\gamma}, \quad X = g_x u_x, \quad \text{and} \quad \Psi = g_y u_y . \tag{2.13b}$$

The domain size L_D is the length ΔY required for $\mathbf{u}(Y)$ to change by one lattice vector $\mathbf{a}_i$; the lateral extent of the domain is L_x. The displacement functions have the following periodicities:

$$X(Y + L_D) - X(Y) = \begin{cases} 0 & \text{(SHW)} \\ \pm\pi & \text{(HW)}, \end{cases}$$

$$\Psi(Y + L_D) - \Psi(Y) = \begin{cases} -2\pi & \text{(SHW)} \\ -\pi & \text{(HW)} , \end{cases} \tag{2.14}$$

where SHW and HW denote the superheavy- and heavy-wall configurations defined[12] in Sec. II C. The signs of the increments in Eqs. (2.14) are reversed for the superlight- and light-wall configurations (SLW and LW).

The energy of one domain of the uniaxially incommensurate layer relative to the energy of the same number of atoms in the commensurate state is

$$\Delta E = \{u_y(L_D) - u_y(0)\}(-L_x\phi) + (V_0 L_x/\sqrt{\gamma})\epsilon . \tag{2.15}$$

The scaled energy ϵ, defined by

$$\epsilon = \int_0^{L_D} dY \left[\tfrac{1}{2}(d_Y\Psi)^2 + (A/2)(d_YX)^2 + 3\cos(\theta) \right.$$
$$\left. -\cos(2X+\theta) - 2\cos(X-\theta)\cos(\Psi) \right] , \quad (2.16)$$

is to be minimized under functional variations of Ψ and X.

The coupled second-order nonlinear differential equations which result from the minimization are

$$-d_Y^2\Psi + 2\cos(X-\theta)\sin(\Psi) = 0 ,$$
$$\quad (2.17)$$
$$-A\, d_Y^2X + 2\sin(2X+\theta) + 2\cos(\Psi)\sin(X-\theta) = 0 ,$$

subject to the boundary conditions in Eq. (2.14). If the pair Ψ, X satisfies Eqs. (2.17), then $-\Psi, X$ does also. Thus the energies ϵ for the HW and LW configurations on a domain L_{HW} are equal, as are the energies ϵ for the SHW and SLW on a domain L_{SHW}.

The energy difference between one SHW on a domain of size L_{SHW} and two HW's in the same total length is proportional to

$$\Delta\epsilon = \epsilon_{SHW}(L_{SHW}) - \epsilon_{HW}(L_{D1}) - \epsilon_{HW}(L_{SHW} - L_{D1}) .$$
$$\quad (2.18)$$

Since the results for ϵ_{HW} satisfy

$$d\epsilon_{HW}(L)/dL \le 0 ,$$
$$\quad (2.19)$$
$$d^2\epsilon_{HW}(L)/dL^2 \ge 0 ,$$

there is a bound

$$\Delta\epsilon \le \Delta\epsilon' = \epsilon_{SHW}(L_{SHW}) - 2\epsilon_{HW}(L_{SHW}/2) . \quad (2.20)$$

When $\Delta\epsilon'$ is negative, the SHW configuration has lower energy than two HW's in the same length L_{SHW}; the corresponding SLW has lower energy than two LW's.

Houlrik and Landau[20] compared the energy of one HW in a length L_{HW} to the energy of one SHW and one LW in the same total length. This amounts to finding the sign of

$$\Delta\epsilon'' = [\epsilon_{HW}(L_{HW}) - \epsilon_{LW}(L_{HW} - L_1)] - \epsilon_{SHW}(L_1) .$$
$$\quad (2.21)$$

The bracketed first term on the right-hand side of Eq. (2.21) is negative, by the first of Eqs. (2.19). For $\theta = 0$, ϵ_{SHW} is shown to be positive by inspection of Eq. (2.16). Thus $\Delta\epsilon''$ is negative for the GR model. Houlrik and Landau made four energy comparisons among the HW, LW, SHW, and SLW for atomistic models of adsorption on graphite; only one detailed calculation, for Eq. (2.20), is needed in the continuum approximation.

E. Small-amplitude vibrations

The normal modes of the nonuniform elastic continuum are obtained by linearization of the dynamical equations derived from the kinetic energy (ρ is the mass density)

$$K = \int d^2r(\rho/2)[(\partial u_x/\partial t)^2 + (\partial u_y/\partial t)^2] \quad (2.22)$$

and the total potential energy, Eqs. (2.1) and (2.8). The scaled displacements $g_x u_x$ and $g_y u_y$ are sums of the static structure functions, Sec. II D, and small-amplitude harmonic oscillations with wave number q for the phasing along the x axis:

$$g_x u_x = X(Y) + \eta(Y)/\sqrt{3}\exp[i(qx - \omega t)] ,$$
$$\quad (2.23)$$
$$g_y u_y = \Psi(Y) + \xi(Y)\exp[i(qx - \omega t)] .$$

The scaled wave number Q and frequency Ω are defined by

$$Q = q/\sqrt{\gamma} ,$$
$$\Omega^2 = \rho\omega^2/\gamma\Gamma_{11} . \quad (2.24)$$

The normal-mode equations become coupled second-order linear differential equations for the functions η and ξ:

$$\Omega^2\xi = -d_Y^2\xi + (AQ^2/3)\xi - iQ[1 - (A/3)]d_Y\eta$$
$$+ 2\cos(X-\theta)\cos(\Psi)\xi$$
$$- (2/\sqrt{3})\sin(X-\theta)\sin(\Psi)\eta$$

and

$$\Omega^2\eta = -(A/3)d_Y^2\eta + Q^2\eta - iQ[1 - (A/3)]d_Y\xi$$
$$+ \tfrac{4}{3}\cos(2X+\theta)\eta + \tfrac{2}{3}\cos(X-\theta)\cos(\Psi)\eta$$
$$- (2/\sqrt{3})\sin(X-\theta)\sin(\Psi)\xi . \quad (2.25)$$

These are ordinarily solved as a matrix eigenvalue problem using a truncated Fourier series

$$\xi(Y) = \sum_{-N}^{N} a_n \exp\{iY[K + n(2\pi/L_D)]\} ,$$
$$\quad (2.26)$$
$$\eta(Y) = \sum_{-N}^{N} b_n \exp\{iY[K + n(2\pi/L_D)]\} .$$

The domain size L_D is defined by Eqs. (2.14); the range of K is

$$-(\pi/L_D) < K \le (\pi/L_D) . \quad (2.27)$$

A zero-frequency solution is constructed by use of Eqs. (2.17): the functions $\xi_0 = d_Y\Psi$ and $\eta_0 = \sqrt{3}d_YX$ satisfy Eqs. (2.25) with $\Omega = Q = 0$. The elastic continuum model has no pinning of the domain walls.[19]

The frequency spectrum of the uniform elastic continuum, no external potential, has two dispersionless acoustic branches with speeds of sound given by Eqs. (2.3). The uniaxially incommensurate monolayer has only one acoustic branch.

Equations (2.25) also result from a functional minimization of a ratio of quadratic forms in ξ and η. This reformulation leads to an upper bound on the speed of long-wavelength transverse waves with trial functions based on the static configuration solution. For $\theta = 0$, a quadratic form for a_2,

$$a_2 = (\Omega/Q)^2 \quad \text{as } Q \to 0 , \quad (2.28)$$

is defined by

$$a_2 = N(\xi,\eta)/D(\xi,\eta) \ , \tag{2.29}$$

with

$$D(\xi,\eta) = \int dY [\xi_0^2 + \eta_0^2] \ , \tag{2.29a}$$

$$N(\xi,\eta) = \int dY \{ (A/3)\xi_0^2 + \eta_0^2 + (d_Y\xi_1)^2 + (A/3)(d_Y\eta_1)^2 - 2[1-(A/3)][\eta_1 d_Y\xi_0 + \xi_1 d_Y\eta_0]$$

$$+ 2\cos(\Psi)\cos(X)[(\xi_1)^2 + \tfrac{1}{3}(\eta_1)^2] + \tfrac{4}{3}\cos(2X)(\eta_1)^2 - (4/\sqrt{3})\sin(\Psi)\sin(X)\xi_1\eta_1 \} \ , \tag{2.29b}$$

where the leading Q dependences are

$$\xi = \xi_0 + iQ\xi_1 \quad \text{and} \quad \eta = \eta_0 + iQ\eta_1 \tag{2.30}$$

and the functions ξ_0 and η_0 are

$$\xi_0 = d_Y\Psi, \quad \eta_0 = \sqrt{3}\, d_Y X \ . \tag{2.30a}$$

An upper bound for a_2 is obtained by choosing

$$\xi_1 = \alpha d_Y\eta_0, \quad \eta_1 = \beta d_Y\xi_0 \tag{2.30b}$$

and minimizing $N(\xi,\eta)$ with respect to variations of α and β. In the case of the GR SHW, with an analytic solution for Ψ, a simplified expression for a_2 is given in Eq. (A8).

III. STATIC CONFIGURATION

The scaled displacement functions Ψ and X, and energy ϵ of the superheavy- (SHW) and heavy-wall (HW) configurations are obtained as a function of the elastic constant ratio A and domain size L_D. The coupled non-linear differential equations, Eqs. (2.17), are integrated with a fourth-order Range-Kutta method. For large L_D, the variation of the functions Ψ and X is concentrated in ranges of Y which are small compared to L_D, and which are taken to be locations of domain walls. In most cases, the symmetry of the solutions permits an identification of the domain-wall center. The wall width is defined[5] by a linear extrapolation from the center to the limiting values of the functions Ψ and X.

The dependence of the energies ϵ_{SHW} and ϵ_{HW} on domain size is described as the interaction of distinct domain walls for large L_D. The wall-wall interactions vary exponentially with L_D, being derived from mechanical energies for the adlayer in a rigid external potential.

The static stability of a SHW relative to separation into two HW's is treated as a function of L_D and A. The analysis transcribes (Sec. II D) to the case of the static stability of a SLW against separation into two LW's.

A. GR model

The static SHW case of the GR model, Eq. (2.17) with $\theta = 0$, reduces to the one-dimensional model of Frank and van der Merwe.[3] The solution is independent of the elastic constant ratio A, and the displacement $\mathbf{u}(Y)$ has one nonvanishing component Ψ. The scaled energy, given in Eq. (A3), is closely approximated for large L_D ($=L_{\text{SHW}}$) by[15]

$$\epsilon_{\text{SHW}}(L_D) - 8\sqrt{2} \approx 32\sqrt{2}\exp(-L_D\sqrt{2}) \ . \tag{3.1}$$

The wall-wall interaction energy is given to better than 5% by the right-hand side of Eq. (3.1) for L_D as small as 2. The solutions for the SHW energy in this paper are obtained by Runge-Kutta integration, and their accuracy is tested by comparing them to the analytic solution Eq. (A3).

The solution of Eqs. (2.17) satisfying the HW boundary condition of Eqs. (2.14) has a vector displacement function $\mathbf{u}(Y)$, with components given by X and Ψ. The function ϵ_{HW} satisfies Eq. (2.19), as shown in Fig. 2(a). The
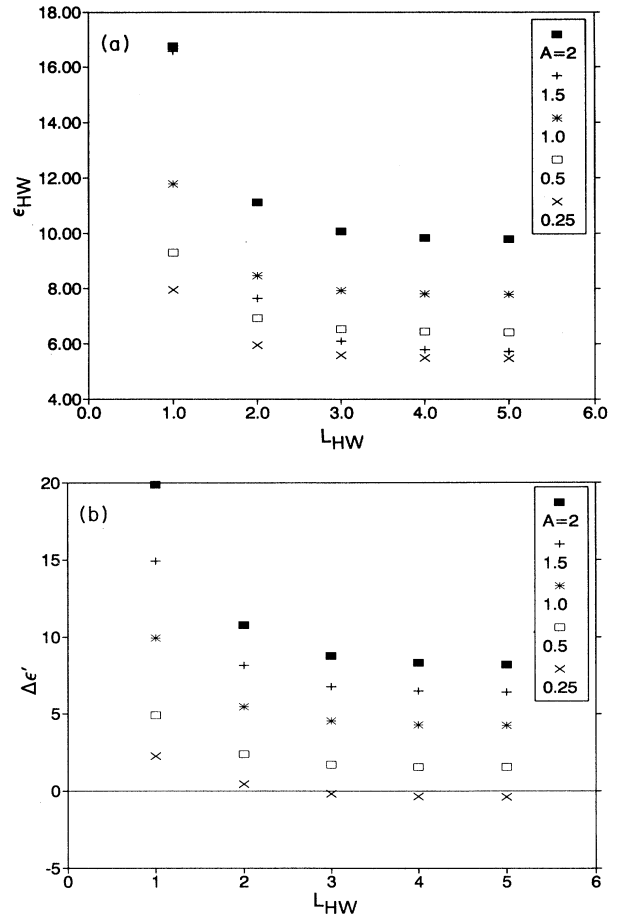

FIG. 2. The scaled energy of the heavy wall (HW) for the GR model as a function of domain size $L_D = L_{\text{HW}}$ for specified values of the elastic constant ratio A. (a) The energy $\epsilon(L_{\text{HW}})$, which has the convexity property stated in Eq. (2.19); (b) the energy differences $\Delta\epsilon'$, Eq. (2.20), of 2 HW and 1 SHW.

difference $\Delta\epsilon'$ is shown in Fig. 2(b); for each value of A, it increases as L_{HW} decreases. Thus, for $A = 0.25$, an array of SHW's at large $L_{SHW} = 2L_{HW}$ has larger energy than the HW array, but the SHW array has smaller energy for $L_{SHW} \leq 5$.

Thermodynamic stability at zero temperature is decided by constructing the enthalpy as a function of the spreading pressure, i.e., the Maxwell double tangent construction, to locate first-order phase coexistence. For $A = 0.25$, the intersection of the mechanical enthalpies for the SHW and HW occurs for $L_{SHW} = 5.2$ and $L_{HW} = 3.1$. The major part of the enthalpy difference of the SHW and HW solids at low spreading pressure is given by the increment defined in Eq. (2.20).

A variational approximation[8] for the HW array at large L_{HW} led to an estimate that the SHW array is stable for $A \geq 0.3$. The interpolation of data corresponding to Fig. 2(b) gives the energy stability for $A \geq 0.295$ at large L_{HW}, in very good agreement. Gordon[16] found stability for $A \geq \frac{1}{3}$ for a slightly different substrate model.

The scaled energy ϵ_{HW} depends approximately exponentially on distance L_{HW}, as shown in Fig. 2(a). Fits for $L_{HW} > 2$ have an exponential scale length which decreases slightly as A increases, and a prefactor which increases as A increases.

By choosing the domains to be $-L_{SHW}/2 < Y < L_{SHW}/2$ for the SHW and $-L_{HW}/2 < Y < L_{HW}/2$ for the HW, symmetric static solutions may be constructed which satisfy

$$\Psi_{SHW}(-Y) + \Psi_{SHW}(Y) = -2\pi ,$$

$$\Psi_{HW}(-Y) + \Psi_{HW}(Y) = -\pi , \qquad (3.2)$$

$$X_{HW}(-Y) + X_{HW}(Y) = -\pi .$$

These properties simplify the matrix form of the normal-mode problem.

The widths of the domain walls centered at $Y = 0$ [Eq. (3.2)] are defined[5] as the ranges ΔY over which a linear extrapolation of the tangent to Ψ at $Y = 0$ goes from 0 to -2π for the SHW and from 0 to $-\pi$ for the HW, $w_{SHW} = 2\pi/\Psi'_0$, and $w_{HW} = \pi/\Psi'_0$. An analytic form for w_{SHW} is given in Eq. (A5). Results are shown in Fig. 3, where the solid line is a limit in which the width ΔY equals the domain size. The widths approach limiting values for large domain size. For $L_D < 1$, ΔY is at least 95% of L_D; thus the variation of Ψ is nearly linear in small domains. The HW width increases as A increases at fixed L_{HW}, and as L_{HW} increases at fixed A. The width $2w_{HW}$ is larger than w_{SHW} when comparisons are made at the same A and the same total misfit, as in Fig. 3.

The ratio of the wall width to the domain size is a guide to understanding the frequency dispersion of normal modes, because it is a measure of the inhomogeneity of the medium in which the waves propagate. It is also a guide to when the incommensurate solid is a nearly uniform solid, and when it has a strongly striped structure with localized domain walls.

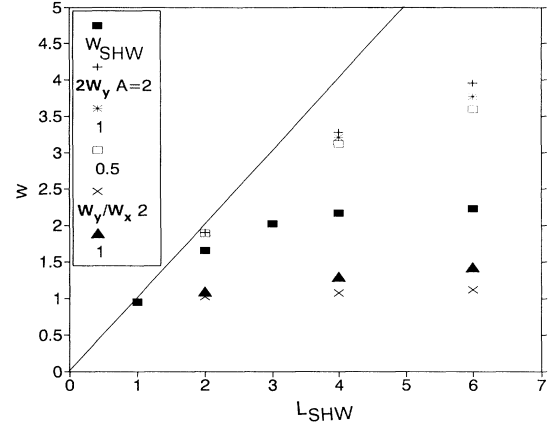An array of HW's parallel to the x axis, as here, is

FIG. 3. Wall widths for the GR model. The wall widths defined in Sec. III A are shown for the SHW and the HW, at specified values of A, as a function of the domain size L_{SHW} of the SHW. The W(SHW) are the SHW widths. The HW widths are plotted as $2W_y$ at $L_D = 2L_{HW}$; thus total widths for the same misfit are compared. The ratio W_y/W_x of the heavy-wall widths in the Y and x displacements, derived from the ratio X'/Ψ' of the slopes at the midpoint of the wall, is shown for specified A. The solid line shows the limit in which the wall width equals the domain size.

lower in energy than the SHW array for A less than 0.3. However, related structures have lower energy than this HW array. The HW array oriented parallel to the y axis is described[7] by equations of the form of Eqs. (2.17), with an effective elastic constant $A' = 9/A$. For $L_D \to \infty$ and A less than 0.55, its energy increment for a given change in adlayer area is lower than that of the SHW array parallel to the x axis. Also, for $L_D \to \infty$, an array of parallel SHW's rotated by a small angle from the x axis is favored relative to this SHW array for A less than 0.62. The onset of the rotation is discussed in Sec. IV A. The effect is similar to one found by Pokrovsky and Talapov[19] for rectangular substrates.

B. fcc(111) model

The displacement function of the fcc(111) model which satisfies the SHW condition in Eq. (2.14) has vector character. This is[6,7] a consequence of the small potential-energy barriers for saddle points between the fcc and hcp sites.

The SHW solution has a symmetry, for $-L_{SHW}/2 < Y < L_{SHW}/2$,

$$\Psi_{SHW}(-Y) + \Psi_{SHW}(Y) = -2\pi ,$$

$$X(-Y) = X(Y) . \qquad (3.3)$$

The solution in the degenerate case, $\psi = 0$, has a further symmetry about each of the saddles which is similar to the HW case of Eq. (3.2).

Results for the scaled energy of the SHW, with $\psi = 0$, as a function of the domain size L_{SHW} are shown in Fig. 4 for several values of A. The values for $L_{SHW} > 20$ are

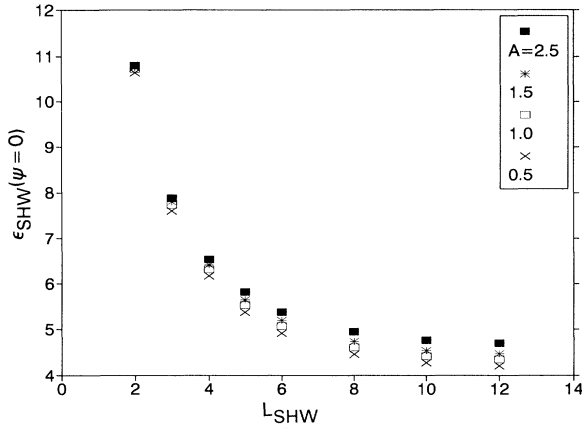FIG. 4. The scaled energy of the fcc(111) SHW as a function of the domain size L_{SHW} for $\psi=0$ and specified values of A.

FIG. 5. The size of the minority domain as a function of the degeneracy parameter ψ for $A=1$ and specified values of domain size L_{SHW}. Data for $A=2$ and 0.5 would scarcely be distinguishable on this graph. The length L_β is the Y range for the domain of the higher-energy stacking sites, measured between saddle points of the potential.

within 0.1% of variational estimates[8] for isolated walls. Values for a given A are fit well by the form

$$\epsilon(L)=\epsilon_\infty+f_A \exp(-\gamma_A L) ; \qquad (3.4)$$

for $A=1$, the parameters of the exponential are $f_A \approx 12$ and $\gamma_A \approx 0.46$. The values of ϵ for values of ψ appropriate to physical adsorption are close to those shown in Fig. 4; for $\psi=0.005$, ϵ increases by 1% at $L=4$ and by 5% at $L=24$.

There are substructures[6-8] resembling domain walls which are centered near the potential-energy saddles between the fcc and hcp sites for large L_{SHW}. For $\psi=0$, the substructures are equally spaced and there is a characteristic extinction of a diffraction structure factor, which has been used[6] to conclude that Xe/Pt(111) deviates strongly from this model. For $\psi \neq 0$ and large L_{SHW}, there are unequal-sized domains[9-11] of atoms centered on fcc and hcp sites.

The SHW solution for $\psi \neq 0$ reflects a balance between wall-wall interactions and the difference in site energies of the two domains. It is treated quantitatively as follows. The saddle point of the potential energy, Eq. (2.12), is used as the demarcation between domains. The increment in Y between the saddles bounding the higher-energy sites is defined to be the size L_β of the minority domain; the lower-energy sites are in a domain of width $L_\alpha=L_{SHW}-L_\beta$. Values of L_β as a function of ψ and L_{SHW} are shown in Fig. 5 for $A=1$. For large L_{SHW}, the value of L_β approaches a finite limit which depends on ψ. The increment in energy is, with a picture of very sharp domain walls with nearest-neighbor exponential repulsions as in Eq. (3.4),

$$\Delta\epsilon=(f_A/2)(\exp[-2\gamma_A L_\alpha]+\exp[-2\gamma_A L_\beta])$$

$$+6L_\beta \sin(\pi/3) \sin(\psi) . \qquad (3.5)$$

Minimizing $\Delta\epsilon$ with respect to L_β at fixed L_{SHW} gives a close fit to the data in Fig. 5 for $L_{SHW} > 10$. For large domains, small values of ψ lead to quite unequal-sized subdomains of hcp and fcc sites, but ϵ is only slightly
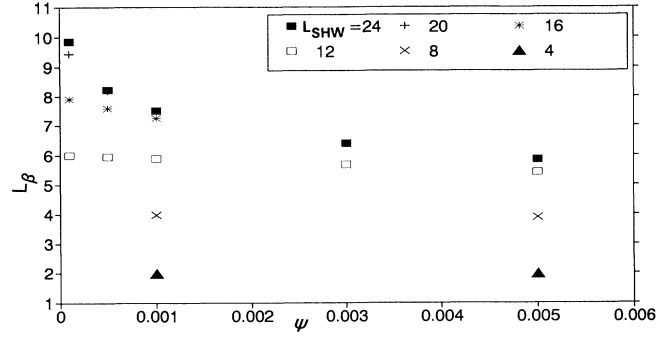
affected. Then a lifting of the structure factor extinction of the degenerate case may be achieved with only a small change in the energy of domain walls.

Wall widths for the fcc(111) model are defined in analogy to those for the GR model (Sec. III A). Results for the $\psi=0$ case are shown in Fig. 6; in this case, the SHW domain has two walls, each of a width $w_Y'=\pi/\Psi_0'$, in terms of the slope of the tangent. For large L_{SHW}, the range of $X(Y)$ in a domain is $\pi/3$, but it can be much less than this at small L_{SHW}. Figure 6 also shows values for the ratio $3X_0'/\Psi_0'$, which is a rough measure of the ratio of the wall widths in Ψ and X.

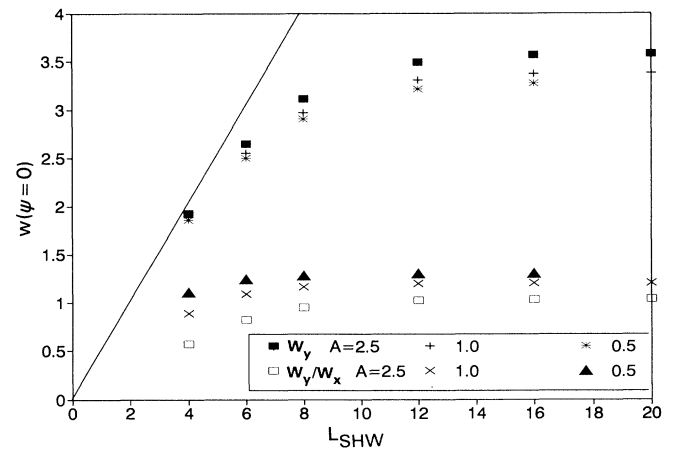The HW of the fcc(111) model is the most complex case treated in this paper. The differential equations are

FIG. 6. Wall widths for the fcc(111) model as a function of L_{SHW} for specified values of A. The SHW widths for $\psi=0$ are derived from the slopes Ψ_0' and X_0' at the saddle point between the two subdomains. The width W_y is defined to be π/Ψ_0'. The ratio W_y/W_x of the wall widths in the displacements u_y and u_x, given approximately by $3 X_0'/\Psi_0'$, is also shown. See Sec. III B for further discussion.

solved on the interval $0 < Y < L_{HW}$ with the initial conditions $X(0)=X_0$ and $\Psi(0)=0$. The initial values of the derivatives are adjusted to make the solution satisfy $X(L_{HW})=X_0-\pi$ and $\Psi(L_{HW})=-\pi$; periodicity in the derivatives is achieved only by a particular choice for X_0. For $\psi=0$, the value is $X_0=\pi/3$; for $\psi\neq0$, the value depends[29] on A and on L_{HW}.

Values for the scaled energy of the HW structure, $\psi=0$, are presented in Fig. 7 as a function of the domain size L_{HW} for several values of A. Again, the dependence on domain size is approximately exponential. An estimate[8] of the HW energy for large L, with the variational functions used for the GR HW, is about 50% higher than the values from the direct numerical solution. These trial functions omit the fact that, as for the SHW structure, the HW misfit involves a spatially varying displacement with atoms near both the hcp and fcc stacking sites.

The conclusion[8] remains that the fcc(111) SHW is stable against separation into HW structures for a wide range of elastic constant ratios A. The ratio $2\epsilon_{HW}(L_{HW})/\epsilon_{SHW}(2L_{HW})$ at $L_{HW}=8$ decreases from 2 at $A=2.5$ to 1.47 at $A=0.5$ and 1.33 at $A=0.25$. If there is a regime where the SHW is energetically unstable relative to the HW, it must involve quite small values of A and large values of L_{HW}. Similarly, the results of Okwamoto and Bennemann[7] show that this SHW is favored over a HW structure formed in uniaxial compression along the x axis (Sec. II C) for large L_D and $A>0.1$; the stability is confirmed here by direct calculation for $A>0.4$.

IV. HARMONIC DYNAMICS

The frequency spectrum of normal modes of the static equilibrium configurations is obtained from Eqs. (2.25). The solutions use matrix diagonalization with the expansion in Eq. (2.26) and Runge-Kutta integrations in special cases. The nonuniform static density distribution implies that there is dispersion in the frequency spectrum. Some
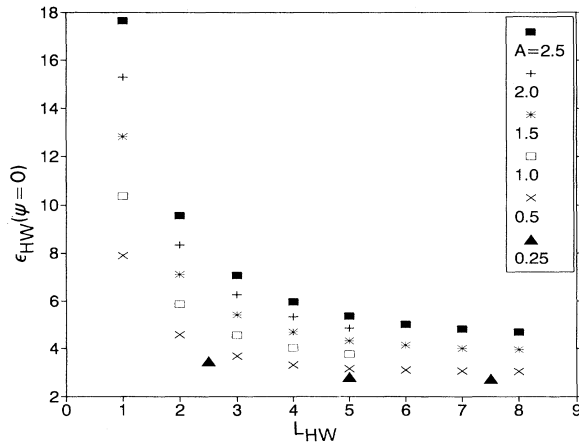

FIG. 7. The scaled energy ϵ_{HW} of the fcc(111) HW as a function of the domain size L_{HW} for $\psi=0$ and specified values of A. In each case $2\epsilon_{HW}(L_{HW})$ is much larger than $\epsilon_{SHW}(2L_{HW})$.

of the SHW spectra have anomalous dispersion, where the frequency dependence on wave number is supralinear. More surprising is that, for both the GR and the fcc(111) models, the SHW stripe is dynamically unstable for ranges of A and L_{SHW} where the SHW has lower energy than the HW stripe.

A. GR model: SHW array

The harmonic-frequency spectra $\Omega(Q,K)$ on a given domain L_D are the same for the SHW and SLW. There are symmetries $\Omega(Q,K)=\Omega(-Q,K)=\Omega(Q,-K)$, so that only the positive quadrant $Q\geq0$ and $K\geq0$ need be treated.

The normal-mode equations for the GR SHW simplify considerably, using $X=\theta=0$ and Eq. (3.2). The frequencies $\Omega=\Omega(Q,K)$ are then the eigenvalues of a real symmetric matrix, because the relation

$$V(m)=(1/L_{SHW})\int_{-L_{SHW}/2}^{L_{SHW}/2}\cos(\Psi)$$
$$\times\exp[i2\pi mY/L_{SHW}]dY$$
$$=(2/L_{SHW})\int_0^{L_{SHW}/2}\cos(\Psi)\cos[2\pi mY/L_{SHW}]dY$$

$$(4.1)$$

reduces the matrix problem arising from Eqs. (2.25) and (2.26). Rather explicit results are available along the axes $Q=0$ and $K=0$.

The lowest-frequency solutions for $Q=0$ are obtained from the second-order differential equation[14]

$$\Omega(0,K)^2\xi=-d_Y^2\xi+2\cos(\Psi)\xi , \qquad (4.2a)$$

where Ψ is the solution of

$$-d_Y^2\Psi+2\sin(\Psi)=0 , \qquad (4.2b)$$

satisfying $\Psi(Y+L)=\Psi(Y)-2\pi$. This problem was solved[14] by Sutherland and by Pokrovsky and Talapov. Sutherland showed that $\Omega(0,K)^2$ has only two bands and that the gap in Ω^2 at $K=\pi/L$ is 2. Pokrovsky and Talapov constructed the small-K solution in terms of integrals of Ψ. Their solution can be expressed in terms of elliptic integrals, Eq. (A6); the large-L limit is

$$\Omega(0,K)^2/K^2=(\omega^2/\gamma K^2)/c_l^2\approx8L^2\exp(-L\sqrt{2}), \quad K\to0.$$

$$(4.2c)$$

This is accurate to 2% at $L=6$. Since the second of Eqs. (2.25) does not map precisely onto the Sutherland solution, there may be (and is) more than one gap in the transverse (η) frequency spectrum.

Equation (4.2) provide a test of the numerical solutions, which include the Bloch-Floquet construction of McMillan[30] and the truncated matrix eigenvalue problem using Eq. (2.26).

A second special case is $K=0$, for which the lowest-frequency motions are transverse oscillations of the domain-wall array. The variational approximation defined in Eqs. (2.29) and (2.30) gives a tight upper bound on Ω at small Q, Eq. (A8). For very large L, it is

$$\Omega(Q,0)^2(3/AQ^2)=(\omega/qc_t)^2=1-\Delta f(A), \quad Q\to 0,$$

$$\Delta f_{\text{var}}=(5/3A)(3-A)^2/(11+7A). \tag{4.3}$$

A direct numerical solution for Δf obtained by scaling Eqs. (2.25) is within 10% of Δf_{var} at $A=1.5$, 5% at $A=1$, and 1% at $A=0.5$. For finite L, the variational bound Eq. (A8) is even tighter. For $A=1$, the bound for $1-\Delta f$ is 1.3% larger than the numerical solution at $L_{\text{SHW}}=4$ and 0.4% larger at $L_{\text{SHW}}=2$.

There are several noteworthy features of Eq. (4.3): (i) the speed of transverse waves (as $Q\to 0$) is independent of the corrugation amplitude V_g; (ii) the propagation of long-wavelength waves may be quite anisotropic, comparing Eqs. (4.3) and (4.2c); and (iii) there is a dynamic instability, $\Omega^2<0$, for small A. At large L_{SHW}, the variational estimate Eq. (4.3) ensures that there is a range of negative Ω^2 for $A<0.617$; a direct solution shows that $\Omega(Q,0)^2<0$ at small Q for $A<0.6219$.

The dynamical instability can be linked to the onset of a rotation of the parallel SHW array relative to the x axis. The static energy for an arbitrary direction $\mathbf{n}$ of uniaxial compression (Sec. II C) is expanded to second order in the (small) rotation angle. The quadratic form is identical to that in Eq. (2.29) for the small-Q limit of $\Omega(Q,0)^2$. Then the condition $a_2<0$ implies that the static energy is lowered by the rotation. Pokrovsky and Talapov[19] treated the rotation on rectangular substrates.

The limit of $\Omega(Q,0)^2$ at large Q and L is

$$\Omega(Q,0)^2(3/AQ^2)\approx 1-(\delta/Q^2), \quad Q\to\infty,$$

with

$$\delta=1+(6/A)-\sqrt{[1+(24/A)]}. \tag{4.4}$$

Thus the phase velocity approaches the speed of transverse sound in the uniform medium.

The transverse wave has anomalous dispersion, i.e., $\omega(q,0)/q$ initially increases as Q increases. Results in Fig. 8 from the direct solution for $\Omega(Q,0)^2$ show the

dynamical instability for small A and the anomalous dispersion. The effect of wall-wall interactions is illustrated in Fig. 9 for several values of L_{SHW} and A, using the coefficient $a_2(L)$ in a fit to the lowest frequency at small Q:

$$(\omega(q,0)/qc_t)^2=a_2+a_4Q^2+0(Q^4). \tag{4.5}$$

The coefficient a_2 increases as L decreases and thus remains positive to smaller A as L decreases. The coefficient a_4 is positive (anomalous dispersion) for all cases represented in Fig. 9. It decreases as L decreases; this is in accord with the increasing uniformity of the medium reflected by the domain-wall widths (Sec. III A). It increases as A decreases and becomes large for small A, as indicated in Fig. 8.

There are phenomenological accounts[19,21] of the transverse vibrations of a domain wall in terms of the line tension and effective mass of a stretched string. The frequencies at small Q can be used to identify the line tension governing small-amplitude vibrations of the wall. Shrimpton and Joos[21] derive an effective mass ρ^* from the kinetic energy by the construction

$$\int d^2r\,\rho(\partial u_y/\partial t)^2\approx\int d^2r\,\rho\{\partial u_y[Y+\xi(t)]/\partial t\}^2$$

$$=\int dx\,\rho^*(d\xi/dt)^2\ ;$$

at finite L, ρ^* is given in Eq. (A7); for $L\to\infty$, it is

$$\rho^*=\rho\int dy(du_y/dy)^2=(8\rho/g_y^2)\sqrt{(2\gamma)}. \tag{4.6}$$

The line tension is defined to be

$$\tau=\rho^*(\omega(q,0)/q)^2, \quad Q\to 0. \tag{4.7}$$

It is distinct from the energy per unit length of a domain wall, which is a combination of the scaled energy ϵ [Eq. (2.16)] and the spreading pressure ϕ [Eq. (2.1)]. The utility of the definitions for τ and ρ^* is unclear, because both quantities vary as L varies. The effective mass ρ^*, the
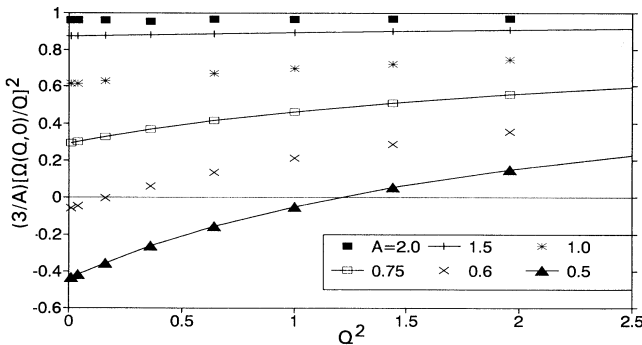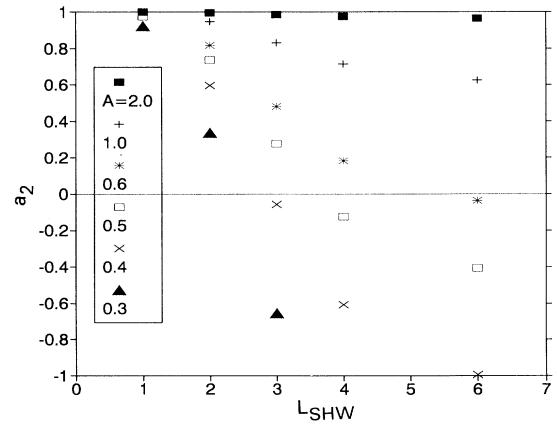

FIG. 8. The dispersion of the lowest-frequency transverse vibration of the GR SHW. The solution for $\Omega(Q,0)$ is plotted in the form $(\omega/qc_t)^2$ vs Q^2 for specified A. In the results shown, for $L_{\text{SHW}}=20$, the effects of wall-wall interactions are very small. The lines join calculated points and are drawn to guide the eye.

FIG. 9. The long-wavelength behavior of the transverse frequency spectrum of the GR SHW. The coefficient a_2, Eq. (4.5), for the small-q limit of $(\omega/qc_t)^2$, is plotted as a function of L_{SHW} for specified A.

speed ω/q, and the line tension all increase as L_{SHW} decreases.

Frequencies at general K and Q are obtained from the matrix eigenvalue problem, Eqs. (2.25) and (2.26). The frequency spectrum is composed of several branches defined on the one-dimensional Brillouin zone, $-\pi/L_{SHW} < K < \pi/L_{SHW}$. There is one acoustic branch, which is a longitudinal acoustic mode for $Q=0$, and a transverse acoustic mode for $K=0$.

The spectrum $\Omega(Q,K)$ enables a generalization of the Debye theory of the specific heat to the case of the nonuniform (striped) lattice. A consequence of the strong anisotropy in the frequency spectrum for large L, Eqs. (4.2) and (4.3), is that the characteristic T^2 variation of the specific heat of the two-dimensional solid is reached only at very low reduced temperatures T^*.

The specific heat for the monolayer solid of area A_0 is

$$C = (A_0 k_B \gamma)/(4\pi^2)$$

$$\times \sum \int_{-\infty}^{\infty} dQ \int_{-\pi/L_{SHW}}^{\pi/L_{SHW}} dK [(\Omega/2T^*)/\sinh(\Omega/2T^*)]^2$$

(4.8)

with reduced temperature $T^* = T/T_0$ and characteristic temperature T_0:

$$T_0 = (\hbar/k_B)\sqrt{(\gamma\Gamma_{11}/\rho)} .$$

(4.9)

The sum in Eq. (4.8) is over branches of the frequency spectrum defined on the first Brillouin zone.

The low-temperature limit of the specific heat is

$$C \approx A_0 k_B \gamma (3\zeta(3)T^{*2})/(\pi c_Q c_K) ,$$

(4.10)

with Riemann zeta function $\zeta(3)$ and speeds c_Q and c_K,

$$\Omega(Q,0) \approx c_Q Q, \quad Q \to 0; \quad \Omega(0,K) \approx c_K K, \quad K \to 0 .$$

The specific heat of a uniform Debye solid, with longitudinal and transverse acoustic branches, is

$$C \approx A_0 k_B \gamma (3\zeta(3)T^{*2})[1+(3/A)]/\pi .$$

(4.11)

The specific heat for $A=1$ is shown in Fig. 10 for a range of temperatures between the low- and high-temperature limits, Eqs. (4.10) and (4.11). The pattern of variation depends on L_{SHW}; C/T^{*2} may have strongly nonmonotonic dependence on T^*. The range of C/T^{*2} is larger for smaller A, but the qualitative pattern for $A=2$ and 0.7 is similar to that shown in Fig. 10. The crossing of the curves in Fig. 10 demonstrates that the specific heat does not vary monotonically with L_{SHW}. First, at very low temperatures, the dominant contribution arises from the low-frequency transverse vibrations of the domain walls; then, at intermediate temperatures, the specific heat for smaller L_{SHW} is enhanced by the narrowing of the gap in the second branch of the spectrum with increasing misfit.

B. GR model: HW array

The spectra $\Omega(Q,K)$ on a given domain L_D are the same for the HW and LW. The symmetry is lower than for the GR SHW: there is inversion symmetry
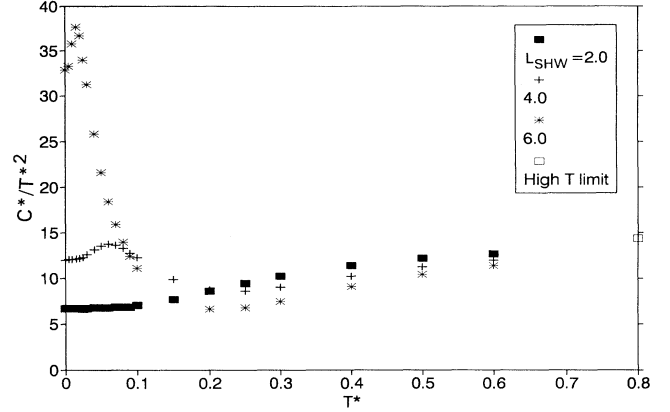

FIG. 10. The specific heat of an elastic solid with a SHW array of the GR type. The quasiharmonic specific heat C for a solid of area A_0 is related to the function C^* by $C = A_0 k_B (\gamma/\pi) C^*$. The ratio C^*/T^{*2}, is plotted as a function of the reduced temperature T^*, Eq. (4.9), for $A=1$ and specified values of L_{SHW}. The $\square$ on the right-hand axis denotes the high-temperature limit, Eq. (4.11), independent of L_{SHW}. The zero-temperature limits are given by Eq. (4.10).

$\Omega(Q,K) = \Omega(-Q,-K)$, but there is no reflection symmetry with respect to the Q axis.

There are notable contrasts to the results for the SHW. No dynamical instability is found, even for ranges of A and L for which the HW array has much larger static energy than the SHW array. The lowest $K=0$ frequency $\Omega(Q,0)$ has normal dispersion with Q.

With the sign conventions used here, at each positive Q there is a minimum frequency at a negative value K (Q) which depends on A and L_{HW}. For $L_{HW} > 4$, the minimum frequency is a few percent lower than the $K=0$ value, but at $L_{HW} = 2$, the reduction is of order 20% for $A < 0.5$.

The $K=0$ spectrum is analyzed for small Q in a similar fashion to Eq. (4.5):

$$\Omega(Q,0)^2/Q^2 = (\omega/qc_l)^2 \approx b_2 + b_4 Q^2, \quad Q \to 0 .$$

(4.12)

The coefficient b_2 is shown in Fig. 11 as a function of L_{HW} for several values of A. The corresponding coefficient b_4 is negative, with a magnitude which varies slowly with L_{HW} and which decreases as A increases.

The variational bound for b_2 obtained from Eqs. (2.29) and (2.30) has an accuracy relative to the direct solution, which improves as L_{HW} decreases at constant A and as A increases at constant L_{HW}. For $A=2$, it is accurate to 1% as L_{HW} ranges from 1 to 16; for $A=1$, the accuracy is 8% at $L_{HW} = 16$ and 0.5% at 1; for $A = 0.25$, the bound is at least 50% above the direct solution for $L_{HW} > 3$ and only 1% larger at $L_{HW} = 1$. The bound is tighter at smaller domain size, where the static density distribution is rather uniform.

C. fcc(111) model: SHW array

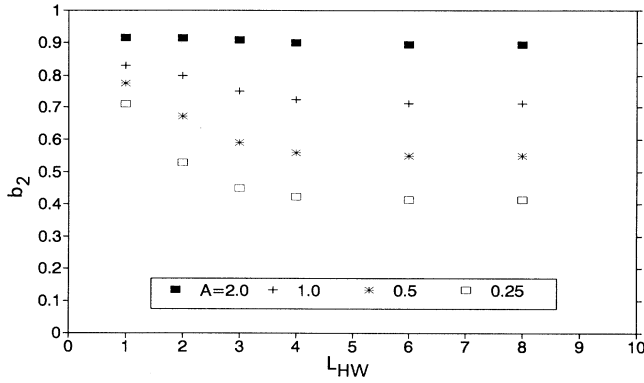The spectra $\Omega(Q,K)$ on a given domain L_D are the same for the SHW and the SLW. There are inversion

FIG. 11. The long-wavelength behavior of the $K=0$ frequency spectrum of the GR HW. The small-Q limit of $\Omega(Q,0)^2/Q^2$, the coefficient b_2 in Eq. (4.12), is plotted as a function of L_{HW} for specified A.

and reflection symmetries: $\Omega(Q,K)=\Omega(-Q,-K)$ $=\Omega(-Q,K)$. There is one acoustic branch in the spectrum, as for the GR SHW.

There are qualitative differences from the spectrum of the GR SHW, which reflect the substructure of the SHW at large L_{SHW} (Sec. III B). The walls between domains of hcp and fcc sites, centered at the two sets of saddles in each domain L_{SHW}, have in-phase and antiphase oscillations. The splitting of the lowest-frequency branches has a dependence on domain size which is in accord with the discussion of Eqs. (3.4) and (3.5):

$$\Delta\Omega^2(Q,0) \propto \exp(-\gamma_A L_{SHW}), \quad \psi=0 , \qquad (4.13a)$$

$$\Delta\Omega^2(Q,0) \propto \exp(-2\gamma_A L_\beta), \quad \psi\neq0 . \qquad (4.13b)$$

That is, for $\psi=0$ the splitting vanishes for $L_{SHW} \rightarrow \infty$. However, for nondegenerate hcp and fcc sites, the splitting remains finite because L_β has a finite limit as $L_{SHW} \rightarrow \infty$.

Information on limiting cases of the fcc SHW spectrum is mostly derived from the numerical solutions. The anisotropy of elastic-wave propagation with wave vectors parallel and perpendicular to the axis of uniaxial compression is demonstrated with phase velocities derived from the lowest-frequency branch according to

$$c_x/c_t = \sqrt{(3/A)} \lim_{Q\to0} \Omega(Q,0)/Q ,$$
$$c_y/c_l = \lim_{K\to0} \Omega(0,K)/K . \qquad (4.14)$$

The ratio $(c_y/c_l)/(c_x/c_t)$ is 1 for the uniform medium; it is exponentially small for a striped structure with widely spaced walls. The dependence on L_{SHW} is shown in Fig. 12 for three values of A, with one case of the GR SHW for contrast. There is a large difference in the L dependence of the fcc and GR models because (i) the walls for the fcc model are effectively at half the spacing for the GR model, as indicated in Eqs. (4.13); and (ii) even after allowing for this difference, the falloff with increasing L is slower for the fcc model because its walls are broader, as reflected in the scale lengths of the exponentials in Eqs. (3.1) and (3.4).
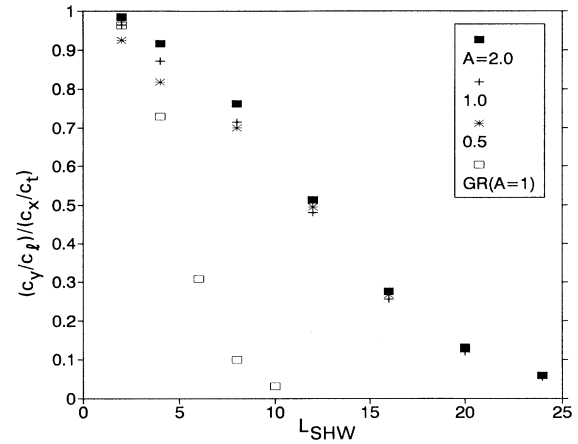

FIG. 12. The anisotropy of the long-wave propagation for the fcc(111) SHW array. The initial slopes of the acoustic branches, c_x for $K=0$ and c_y for $Q=0$ are combined to form $(c_y/c_l)/(c_x/c_t)$, which is plotted as a function of L_{SHW} for three values of A. The corresponding ratio for the $A=1$ case of the GR SHW is shown ($\square$) for contrast.

There appears to be a dynamical instability of the fcc SHW at small A, analogous to that for the GR SHW. Figure 13, which is the analog of Fig. 9, shows the variation of a_2 [Eq. (4.5)] with A and L_{SHW}. The threshold of the instability, extrapolating to $a_2=0$, is $A_c=0.23$ for $L_{SHW}=16$ and $A_c=0.18$ for $L_{SHW}=12$. In contrast to the GR case, no solutions with negative Ω^2 were constructed: the numerical solutions of Eqs. (2.17) are extremely sensitive to initial conditions as the parameters corresponding to the extrapolated threshold are approached. Also, in contrast to the GR case, there is a maximum value (greater than 1) in the variation of a_2
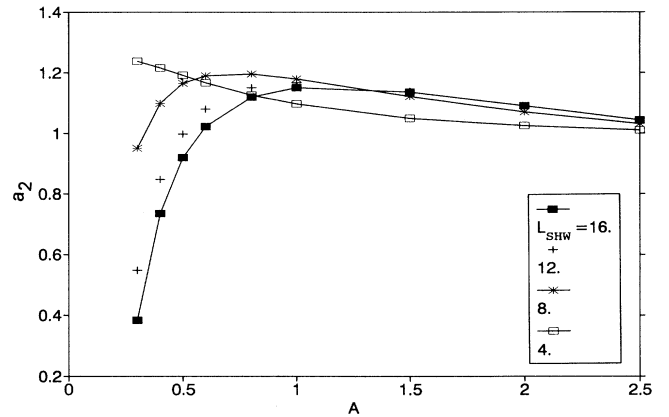

FIG. 13. The long-wavelength behavior of the transverse frequency spectrum of the fcc(111) SHW, for degenerate fcc and hcp stacking sites, $\psi=0$. The coefficient a_2 [Eq. (4.5)] is plotted as a function of elastic constant ratio A for specified values of L_{SHW}. The value of a_2 changes little when ψ is increased to 0.005. The lines join calculated points and are drawn to guide the eye.

with A at fixed L_{SHW}.

There is a range of parameters with anomalous dispersion, $a_4 > 0$ in Eq. (4.5). For $A = 0.5$, the range $L_{SHW} \geq 12$ has $a_4 > 0$. The anomalous dispersion sets in at smaller L_{SHW} for smaller A; a_4 decreases and changes sign as L_{SHW} decreases at constant A. The magnitude of a_4 is smaller and has a slower variation with L_{SHW} than the coefficient for the GR SHW in corresponding ranges of A and L_{SHW}.

Several branches of the frequency spectrum $\Omega(0, K)$ are shown for the fcc(111) SHW, $A = 1$, and $L_{SHW} = 8$, in Fig. 14. The lowest branch is primarily a longitudinally polarized mode, with the ξ component as the dominant part of the eigenvector. In higher branches, the dominant component of the polarization varies as K varies. For $\psi = 0$, the lowest branch would unfold to give a spectrum without gaps on the range $0 < K < 2\pi / L_{SHW}$. This is because the Y dimension of the distinct space lattice unit cell is $L_{SHW}/2$ when the hcp and fcc sites are degenerate. The spectrum in Fig. 14 for $\psi = 0.005$ has small gaps at $K = \pi / L_{SHW}$, consistent with the larger unit cell. The gap for the lowest branch increases with increasing L_{SHW}.

D. fcc(111) model: HW array

The spectra for the HW and the LW on a given domain L_D are related by $\Omega(Q, K)_{HW} = \Omega(-Q, K)_{LW}$. There is inversion symmetry but not reflection symmetry, $\Omega(Q, K) = \Omega(-Q, -K)$, as in Sec. IV B.

The fcc HW is unstable in energy with respect to the SHW for all the conditions explored in these numerical studies. However, no dynamical instability of its harmonic-frequency spectrum is found for static solutions with L_{HW} in the range 1–18 for $A = 2$, 1–16 for $A = 1$, and 1–10 for $A = 0.5$. Finding solutions is limited at the largest L by an extreme sensitivity to the initial conditions in the integration and a consequent problem in
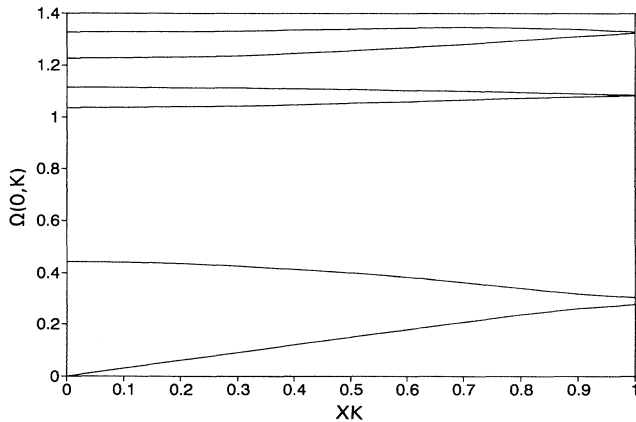

FIG. 14. The frequency spectrum for the fcc(111) SHW with $Q = 0$. Several branches of the frequency spectrum $\Omega(0, K)$ are plotted in the upper half of the first Brillouin zone. The abscissa XK is related to K by $XK = (KL_{SHW})/\pi$. The spectrum shown is for $A = 1$, $L_{SHW} = 8$, and $\psi = 0.005$.

satisfying precisely the boundary condition Eq. (2.14). Correlated with this is the onset of a strong curvature in the dependence of $\Omega(Q, 0)^2 / Q^2$ on Q at small Q. That is, fitting with Eq. (4.12) reproduces the spectrum for Q up to 0.4 at $L_{HW} = 4$, but only for Q up to 0.05 at $A = 1$, $L_{HW} = 12$. The coefficient b_2 [Eq. (4.12)] has behavior similar to that in Fig. 11 for the GR HW. The coefficient b_4 is negative, normal dispersion.

The minimum frequency at given Q occurs for $K \neq 0$, as for the GR HW. The topography of the $\Omega(Q, K)$ surface is more complex than for the GR HW and the minimum frequency at $Q > 0$ does not remain in one quadrant for all the cases. For the cases treated, the reduction from $\Omega(Q, 0)$ ranges up to 40%; the largest effects are for $A = 0.5$, L_{HW} in the range 4 to 10, and $Q < 0.2$.

Lifting the degeneracy of the fcc and hcp sites, up to $\psi = 0.005$, does not change qualitative aspects of the spectrum.

To summarize, no dynamic instability $\Omega^2 < 0$ is found in the fcc HW cases surveyed here; there is no indication that an extrapolation would lead to such a case.

V. CONCLUDING REMARKS

The elastic continuum theory provides a framework for qualitative and semiquantitative discussions of several signatures in observations of uniaxially incommensurate monolayer solids. It helps to put observations and models in a broader perspective. The GR SHW case has immediate application to hydrogen/graphite[22] and helium/graphite, and probably[6,31] to Xe/Pt(111).

The superheavy walls (SHW's) defined by Kardar and Berker[12] are aligned parallel to a pair of reciprocal-lattice vectors of the GR surface. The results of Sec. IV A show that they are dynamically stable for elastic constant ratio $A > 0.62$ at very small misfit, and to smaller values of A for larger misfit (smaller wall spacings). The results of Sec. III A show that the dynamical instability at small A corresponds to a rotation of the axis of the parallel walls, an effect also found by Pokrovsky and Talapov.[19] The elastic constant ratio for helium/graphite is inferred to be in the range $A < 0.7$, using the work of Greif and Goodstein[17] and also using a combination of their work with that of Greywall.[25] Thus a SHW phase of helium/graphite may be preempted by a rotated uniaxially incommensurate lattice. However, the derivation of A from the data[17,25] is based on expressing the Debye temperature and bulk modulus in terms of uniform lattice elastic constants. There is not yet a self-consistent analysis of the helium data which includes the lowering of the effective Debye temperature by domain-wall excitations at small misfit, illustrated in Fig. 10.

Heavy-wall (HW) structures have been defined[12] in which the misfit which would be due to a SHW is achieved by subdivision into two domain walls, each with two-component displacement vectors. The relative energies of HW and SHW lattices with axes parallel to substrate reciprocal-lattice vectors have been calculated previously[8,16,20] and in Sec. III. The aligned HW lattice has the lower energy at a small elastic constant ratio, but a rotated uniaxially incommensurate solid appears to have

still lower energy. The HW lattice has been suggested[25] to occur for ^{4}He/graphite, by associating the average density of a specific-heat signature with a striped structure. The stability of an aligned HW lattice would, on the basis of the present work, be attributed to effects of atomic discreteness which are omitted from the continuum models.

The uniaxially incommensurate solid has one rather than two acoustic branches, but it may have a Debye (T^2) temperature dependence at sufficiently low temperatures. The strong anisotropy of elastic-wave propagation in the solid at small misfits, discussed in Sec. IV and illustrated in Fig. 12, causes this T^2 regime to be reached only at very low temperatures. The model calculations, as in Fig. 10, show that the ratio of the specific heat to the square of the temperature decreases, as the temperature decreases, to a value less than that inferred from the uniform lattice elastic constants. It then increases to a finite limit with further decrease in temperature. This last rise reflects the domain-wall excitations and occurs at temperatures less than 10% of $\hbar\Omega_0/k_B$, where Ω_0 is the angular frequency of the Brillouin-zone center gap of the commensurate lattice. Discreteness effects, such as the Peierls pinning of domain walls, would limit the extent of the rise at low temperature. There has been no interpretation of specific data for striped lattices in such terms: the model calculations indicate the effects may be prominent at low temperatures and small misfits.

The monolayer solid of Xe/Pt(111) is an anomalous physisorption system. Diffraction data[23] for the incommensurate solid have been interpreted[6] as excluding the fcc(111) model with degenerate hcp and fcc stacking sites. Two classes of interaction model had been proposed, one[6,31] with adsorption sites atop surface platinum atoms and one[32] with the diffraction signature attributed to a slight breaking of the degeneracy of the hcp and fcc sites. Small differences in the energy at the fcc and hcp sites lead to unequal-sized subdomains, as discussed in Sec. III B and illustrated in Fig. 5. There are also consequences to the excitation spectrum, as discussed in Sec. IV C. To use the data of Kern *et al.*[23] to distinguish between the two classes of interaction model will require quantitative analysis of the atomic diffraction intensities. However, the result may be a fitted value for the amount of the energy difference between the hcp and fcc sites, with a conclusion depending on how plausible the fitted value appears in the light of modeling of the interactions.[9,10]

There are several examples of anomalous frequency dispersion in the elastic continuum theory, shown for the GR model in Fig. 8 and discussed for the fcc(111) model in Sec. IV C. How much of this can be attributed to the omission of anharmonicity in adatom-adatom interactions will become clearer as further calculations are made with atomistic models.

The interaction energy of parallel domain walls varies exponentially with distance at large separations in this approximation. It is not yet known how the parameters in the dispersion relation of domain walls with large meanders[18,19] are related to the small-amplitude vibrations theory and hence how the entropic interaction[18,19] depends on the elastic constants and corrugation. From that, the relative sizes in a physisorbed system at finite misfit of the exponential interaction, the entropic interaction, and the elastic interaction[9] through a deformable substrate might be determined.

APPENDIX A: ANALYTIC RESULTS FOR THE GR SHW

Frank and van der Merwe[3] expressed solutions of the nonlinear differential equation

$$-d_Y^2\Psi + 2\sin(\Psi) = 0 \tag{A1}$$

in terms of elliptic integrals. Their results transcribe to the GR SHW [Eq. (2.17)] with $X = \theta = 0$. An extension gives expressions for the domain size, energy, elastic wave speed, and effective mass in terms of complete elliptic integrals of the first and second kind, $K(\mu)$ and $E(\mu)$.

The domain width and scaled energy, Eq. (2.15), are given parametrically by

$$L = \sqrt{(2\mu)}K(\mu) , \tag{A2}$$

$$\epsilon = 4\sqrt{(2/\mu)}\{2E(\mu) - (1-\mu)K(\mu)\} . \tag{A3}$$

The contribution of ϵ to the spreading pressure is

$$\Delta\phi = -d\epsilon/dL = 4(1-\mu)/\mu . \tag{A4}$$

The wall width defined in Sec. III A is

$$w = 2\pi/\Psi_0' = 2\pi\sqrt{(\mu/8)} . \tag{A5}$$

The speed of longitudinal waves along the y axis [Eq. (4.2c)] derived from the initial slope of $\Omega(0,K)$ is[14]

$$(c_y/c_l)^2 = (1-\mu)[K(\mu)/E(\mu)]^2 . \tag{A6}$$

The effective mass[21] [Eq. (4.6)] is

$$\rho^* = (8\rho/g_y^2)\sqrt{(2\gamma/\mu)}E(\mu) . \tag{A7}$$

The variational theory for the transverse elastic wave speed, constructed from Eqs. (2.28)–(2.30), is obtained by minimizing the following quadratic form with respect to α:

$$\tfrac{1}{2}(c_x/c_l)^2 I_1 = (A/6)I_1 + \alpha[1 - (A/3)]I_2$$
$$+ \alpha^2[(A/6)I_6 + \tfrac{2}{3}I_2 + \tfrac{1}{3}I_4] , \tag{A8}$$

where

$$I_1 = 8\sqrt{(2/\mu)}E(\mu) ,$$

$$\tfrac{3}{2}I_2 = (4/\mu)^2(\mu-1)L + [(2/\mu)-1]I_1 ,$$

$$\tfrac{5}{4}I_4 = [(2/\mu)-1]I_2 - \tfrac{1}{2}I_1 ,$$

$$I_6 = 2I_1 - I_4 .$$

The expression in Eq. (4.3) is obtained from Eq. (A8) in the limit $L \to \infty (\mu \to 1)$.

[1]J. Villain and M. B. Gordon, Surf. Sci. **125**, 1 (1983).

[2]T. A. Kontorova and Ja. I. Frenkel', Zh. Eksp. Teor. Fiz. **8**, 89 (1938); R. Currat and T. Janssen, Solid State Phys. **41**, 201 (1988).

[3]F. C. Frank and J. H. van der Merwe, Proc. R. Soc. London Ser. A **198**, 205 (1949).

[4]S. C. Ying, Phys. Rev. B **3**, 4160 (1971).

[5]M. B. Gordon and F. Lancon, J. Phys. C **18**, 3929 (1985); R. J. Gooding, B. Joos, and B. Bergersen, Phys. Rev. B **27**, 7669 (1983).

[6]J. M. Gottlieb, Phys. Rev. B **42**, 5377 (1990); J. M. Gottlieb and L. W. Bruch, *ibid*. **44**, 5750 (1991).

[7]Y. Okwamoto and K. H. Bennemann, Surf. Sci. **186**, 511 (1987), treat uniaxially incommensurate solids derived from the 1×1 commensurate adlayer on a fcc(111) substrate, with $\psi = 0$. Their structure I corresponds to the fcc SHW here. The combination of their structures II and III corresponds to the fcc HW here, with an effective elastic constant ratio $A' = 9/A$.

[8]L. W. Bruch, Surf. Sci. **250**, 267 (1991).

[9]S. Narasimhan and D. Vanderbilt, Phys. Rev. Lett. **69**, 1564 (1992), attribute a large-scale herringbone structure of nearly parallel walls to an elastic interaction via the substrate. They use a model corresponding to Eq. (2.10), with $\psi = 0.06$.

[10]R. Ravelo and M. El-Batanouny, Phys. Rev. B **40**, 9574 (1989). Their model for adsorption on fcc(111) has $\psi = 0.004$, a large value for the Lennard-Jones potential which arises from a special truncation they used.

[11]P. Zeppenfeld, G. Comsa, and J. A. Barker, Phys. Rev. B **46**, 8806 (1992).

[12]M. Kardar and A. N. Berker, Phys. Rev. Lett. **48**, 1552 (1982).

[13]N. D. Shrimpton, B. Joos, and B. Bergersen, Phys. Rev. B **38**, 2124 (1988).

[14]V. L. Pokrovsky and A. L. Talapov, Zh. Eksp. Teor. Fiz. **74**, 1102 (1978) [Sov. Phys. JETP **47**, 579 (1978)]; B. Sutherland, Phys. Rev. A **8**, 2514 (1973).

[15]J. Villain, in *Ordering in Strongly Fluctuating Condensed Matter Systems,* edited by T. Riste (Plenum, New York, 1980).

[16]M. B. Gordon, Phys. Rev. B **35**, 2052 (1987).

[17]J. M. Greif and D. L. Goodstein, J. Low Temp. Phys. **44**, 347 (1981).

[18]S. N. Coppersmith, D. S. Fisher, B. I. Halperin, P. A. Lee, and W. F. Brinkman, Phys. Rev. B **25**, 349 (1982).

[19]V. L. Pokrovsky and A. L. Talapov, *Theory of Incommensurate Crystals* (Harwood, London, 1984).

[20]J. M. Houlrik and D. P. Landau, Phys. Rev. B **44**, 8962 (1991).

[21]N. D. Shrimpton and B. Joos, Can. J. Phys. **68**, 587 (1990).

[22]J. Cui, S. C. Fain, Jr., H. Freimuth, H. Wiechert, H. P. Schildberg, and H. J. Lauter, Phys. Rev. Lett. **60**, 1848 (1988).

[23]R. Kern, R. David, P. Zeppenfeld, R. Palmer, and G. Comsa, Solid State Commun. **62**, 391 (1987).

[24]V. Frank, H. J. Lauter, and P. Leiderer, Jpn. J. Appl. Phys. **26**, Suppl. 3, 347 (1987).

[25]D. S. Greywall (unpublished).

[26]J. V. Barth, H. Brune, G. Ertl, and R. J. Behm, Phys. Rev. B **42**, 9307 (1990); A. R. Sandy, S. G. J. Mochrie, D. M. Zehner, K. G. Huang, and D. Gibbs, *ibid*. **43**, 4667 (1991).

[27]A. Erbil, A. R. Kortan, R. J. Birgeneau, and M. S. Dresselhaus, Phys. Rev. B **28**, 6329 (1983).

[28]F. C. Motteler, Ph.D., University of Washington-Seattle, 1986; densities $0.08-0.09/\text{Å}^2$.

[29]A puzzle remains: four conditions at $Y = L$, the values for X, Ψ, $d_Y X$, and $d_Y \Psi$ are satisfied by adjusting three parameters at $Y = 0$, X_0, $d_Y X$, and $d_Y \Psi$. For $\psi = 0$, the solution exploits a symmetry about the saddle between fcc and hcp sites, but for $\psi \neq 0$, there is not a recognized symmetry, which helps to achieve the solution.

[30]W. L. McMillan, Phys. Rev. B **16**, 4655 (1977).

[31]J. A. Barker and C. T. Rettner, J. Chem. Phys. **97**, 5844 (1992).

[32]P. A. Rejto and H. C. Andersen (unpublished).